Available online at www.sciencedirect.com
SCIENCE DIRECT
Polymer 46 (2005) 8734–8744
polymer
www.elsevier.com/locate/polymer

Transitions from solid to liquid in isotactic polystyrene studied by thermal analysis and X-ray scattering

Hui Xu, Peggy Cebe*

Department of Physics and Astronomy, Tufts University, Medford, MA 02155, USA

Received 14 October 2004; received in revised form 9 December 2004; accepted 19 January 2005
Available online 1 July 2005

Abstract

A three-phase model, comprising mobile amorphous fraction (MAF), rigid amorphous fraction (RAF) and crystalline fraction (*C*), has been applied to interpret the thermal transitions and structure of cold-crystallized isotactic polystyrene (iPS) from below the glass transition temperature, T_g, to above the melting point. Quenched amorphous iPS films were isothermally crystallized at different temperatures for 12 h. The fraction of crystalline phase, ϕ_c, was measured by differential scanning calorimetry (DSC), wide angle X-ray scattering and Fourier Transform infrared spectroscopy. The fraction of the mobile amorphous phase, ϕ_{MAF}, was obtained from the heat capacity increment at the glass transition temperature. In the three-phase model, the fraction of the rigid amorphous phase, ϕ_{RAF}, was found from $1-\phi_{MAF}-\phi_c$. Specific heat capacity measurements by standard DSC confirm that the experimental baseline heat capacity conforms to a three-phase model for temperatures ranging from below T_g, up to the relaxation of RAF. The relaxation of RAF appears as a sigmoidal change in heat capacity accompanied by excess enthalpy, in which solid-like RAF is converted to an identical amount of liquid-like MAF.

At temperatures above the relaxation of RAF, either one or two major crystal melting endotherms are observed in standard DSC, dependent upon crystallization temperature. However, using quasi-isothermal temperature modulated DSC, we always observed two reversing melting endotherms. The effects of annealing on iPS structure during the quasi-isothermal measurement were assessed using small angle X-ray scattering (SAXS). Combining the DSC and SAXS results, a model for the melting of iPS lamellae at low heating rates is presented.

Keywords: Isotactic polystyrene; Heat capacity; X-ray scattering

1. Introduction

In our previous study on well-crystallized bulk film of isotactic polystyrene, iPS, we found the coexistence of three fractions, viz. the crystalline fraction, *C*, the rigid amorphous fraction, RAF, and the mobile amorphous fraction, MAF [1–3]. Like other semicrystalline bulk polymers (e.g. poly(ethylene terephthalate), PET [4], poly(butylene terephthalate), PBT [5], poly(etheretherketone), PEEK [6,7], poly(phenylene sulfide), PPS [8,9], and polycarbonate, PC [10], in cold crystallized iPS only the mobile amorphous fraction participates in the glass transition and becomes liquid-like just above T_g, the glass transition temperature. The crystalline and rigid amorphous fractions maintain their solid character within a certain temperature range above T_g. Below T_g, all three of the phase fractions behave as solid-like; above the final melting temperature of the crystals, all the material is disordered liquid melt.

In well-crystallized iPS bulk film, the rigid amorphous fraction was established at the crystallization temperature (T_c) [1], and most of the RAF develops during secondary crystallization in a manner parallel to the development of the crystalline phase [2,3].

A standard DSC scan of an iPS bulk film crystallized at low T_c ($T_c = 140\ ^\circ C$) shows three endothermic peaks [1]. The lowest one, termed the 'annealing peak', was confirmed by heat capacity measurements to be associated with relaxation of RAF. The other two endotherms, occurring at higher temperature than the annealing peak, are due to the melting of crystals [1]. In our previous work, we used quasi-isothermal temperature modulated differential scanning

* Corresponding author. Tel.: +1 6176273365; fax: +1 6176273744.
E-mail address: peggy.cebe@tufts.edu (P. Cebe).

0032-3861/$ - see front matter © 2005 Elsevier Ltd. All rights reserved.
doi:10.1016/j.polymer.2005.01.105

calorimetry (TMDSC) measurements to reveal existence of two small reversing melting peaks, each one occurring in association with one of the crystal melting endotherms seen in standard DSC. Observation of double reversing melting in iPS [1] supports Petermann's proposal that double melting peaks are due, in part, to dual thermal stability distribution along one single lamella [11].

There are still some issues we did not resolve in our previous work. The first question concerns the location of the endotherm called the 'annealing peak' in relation to the crystal melting endotherms. Previously, in the case of relatively high cold-crystallization temperature (170 °C), the annealing peak overlapped with the first melting endotherm of the crystals and could not be separately distinguished [1]. Upon going to relatively low cold-crystallization temperature (140 °C), the relaxation of RAF could be well separated from melting of crystals, but then only one single major melting peak could be seen in a standard DSC scan. Here, by extending the range of crystallization temperatures, we are able to produce the three fractions in iPS such that not only is the relaxation of RAF distinguished from melting, but also the dual endothermic features are clearly maintained [1].

The second question we address in the present work is the role of annealing upon the crystal lamellae during the quasi-isothermal TMDSC experiments. The quasi-isothermal measurements always show a dual reversing melting signature for iPS sample regardless of the cold-crystallization temperature. This observation needs to be reconciled with the fact that only one major melting peak is observed in the standard DSC scan, for iPS cold-crystallized at lower temperatures.

Third, our observations of dual reversible melting in quasi-isothermal TMDSC experiments support Petermann's proposal that the dual melting is due to melting of different portions of lamellae caused by dual thermal stability distribution [11]. However, this suggestion still does not explicitly explain the phenomenon that the temperature of the uppermost endotherm T_{m2} is independent of the cold-crystallization temperature.

In this work, we produce iPS samples cold-crystallized over a wider temperature range so that we can obtain a system to demonstrate relaxation of RAF well separated from the two endotherms indicating melting of crystals. The thermal transitions of RAF and the crystalline fraction, from solid-like to liquid-like, are studied using quasi-isothermal temperature modulated differential scanning calorimetry (TMDSC), standard DSC, and small angle X-ray scattering (SAXS). By combining the special technique of interrupted quasi-isothermal TMDSC with real time SAXS, we study the changes of iPS lamellar structure within the melting region of iPS.

Lamellar thickening during heating recently has been studied by several groups. Crist [12] analyzed the SAXS data using different melting models to explore the melting behavior of poly(ethylene naphthalene 2,6-dicarbonate), PEN. Using the one-dimensional electron density correlation function and the interface distribution function, he suggested that lamellar thickening, melting/reorganization possibly are responsible for the SAXS features demonstrated during heating, for the PEN sample crystallized at lower temperature. Kong and Hay [13] used DSC and TMDSC to investigate the melting behavior of poly(ethylene terephthalate), PET. They attributed the triple endotherms to the melting of secondary and primary lamellae produced during crystallization, and to thickened lamellae produced during heating to the melting point. Matsuda, et al. [14] combined techniques of transmission electron microscopy (TEM) and DSC to study the annealing of solution-crystallized linear polyethylene. Their results show that the annealing at lower temperature slowly thickens the lamellae without melting crystals, while annealing at higher temperatures results in rapid thickening with cooperative partial melting. In this study, we confirm the effects of annealing during heating. The melting of iPS crystals is a complex process involving partial melting, rearranging (annealing), reorganization (recrystallization) and then fully melting.

2. Experimental section

Isotactic (90%) polystyrene powder with a weight–average molecular weight of 400,000 g/mol was purchased from Scientific Polymer Products, Inc. The iPS powder was compression molded at 250 °C for 3 min, then quenched into cold water to obtain the amorphous bulk films. These films were isotropic when observed between crossed polarizers. The amorphous samples were isothermally cold crystallized for 12 h in an oil bath which has been set to the desired crystallization temperatures (T_c): 140, 150, 155, 160, or 165 °C. Argon protection gas was used to prevent oxidation during crystallization.

A TA Instruments temperature-modulated DSC (TA 2920 MDSC) was used for all the thermal measurements. Cooling was accomplished by a TA Instruments Liquid Nitrogen Cooling Accessory (LNCA). The dry nitrogen gas was purged into the TMDSC cell with a flow rate of 20 ml/min. The temperature of the TMDSC instrument was initially calibrated in the standard DSC mode by using the onset of the melting peak for indium at a heating rate of 10 °C/min. Heat flow amplitude calibration was accomplished both by standard DSC and quasi-isothermal TMDSC by using a 27.25 mg sapphire standard. The sapphire, indium and iPS were encapsulated in Al pans. The experimental details about quasi-isothermal TMDSC and DSC have been described in prior Refs. [1,15–17].

Wide angle X-ray scattering (WAXS) patterns of iPS samples were obtained at room temperature from the center surface area of samples using a Philips PW3020 diffractometer (wavelength = 0.154 nm). The scans were taken in $2\theta - \theta$ reflection mode. The scan range of two-theta is from

5 to 35° at a scan rate of 0.5°/min. The crystallinity index was determined from the ratio between the integrated Lorentz-corrected intensity in the crystalline peaks, after subtraction of amorphous background, to the total area of coherent scattering [18,19]. We calculated the contribution of the amorphous phase at each crystallization time by first multiplying the initial amorphous scattering profile (at crystallization time, $t_c=0$) by a reduction factor and then shifting the scaled amorphous pattern along the intensity axis until a good fit was achieved.

Real time, simultaneous WAXS and SAXS experiments were performed in transmission mode at Brookhaven National Laboratory, National Synchrotron Light Source (NSLS) at the X27C beamline. Two one-dimensional gas filled wire detectors were used for WAXS and SAXS data collection. The wavelength, λ, was 0.1371 nm and the scattering vector, q ($q=4\pi \sin\theta/\lambda$, for θ the half-scattering angle) was calibrated using silver behenate for SAXS, and sodelite and silicon for WAXS. Scattering patterns were recorded every 300 s in stepwise annealing experiments, and heating was accomplished using a Mettler hot stage.

The raw intensity data were corrected for detector linearity, sample absorption, background scattering, and changes in incident beam intensity. At large scattering vector, the intensity data are also corrected for deviations from Porod's Law caused by thermal density fluctuations. The correlation function $K(z)$ was then calculated from the Lorentz corrected intensity using [20,21]:

$$K(z) = \int_0^\infty I(q)q^2 \cos(2\pi qz)\mathrm{d}z \tag{1}$$

where z is a dimension parallel to the lamellar stack normal. $K(z)$ is used to obtain the average structural parameters according to the method of Strobl and Schneider [21]. Fig. 1 shows a typical example of the correlation function $K(z)$, for iPS cold-crystallized at 140 °C for 12 h, illustrating determination of the long period L^{MAX} and smaller phase thickness z_2. The larger correlation phase thickness, z_1, is found from:

$$z_1 = L^{MAX} - z_2 \tag{2}$$

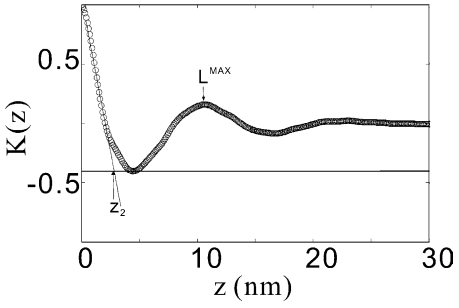

Fig. 1. One-dimensional electron density correlation function, $K(z)$ vs. z, normalized to unity at $z=0$ for iPS cold-crystallized at 140 °C for 12 h, showing the determination of L^{MAX} and the smaller correlation thickness, z_2.

The scattering invariant, Q, is calculated from [22]:

$$Q = \int_0^\infty I(q)q^2\mathrm{d}q \tag{3}$$

For a two-phase system Q is also written [22]:

$$Q \sim \phi_s\phi_c(1-\phi_c)(\Delta\rho)^2 \tag{4}$$

where ϕ_c and $(1-\phi_c)$ are, respectively, the volume fractions of the crystalline and non-crystalline phases within lamellar stacks; ϕ_s is the spherulite filling fraction. The scattering contrast factor, $\Delta\rho$, is the density difference between the crystalline and non-crystalline phases measured in electrons per unit volume. Absolute intensities were not measured and so Q is not placed on an absolute scale. A remark is needed about the use of the two-phase structural model for iPS. The rigid amorphous fraction is treated structurally as a part of the non-crystalline phase. Whereas the RAF can be distinguished as a third component in heat capacity measurements, only the crystalline fraction, ϕ_c, and non-crystalline fraction, $1\text{-}\phi_c=\phi_{MAF}+\phi_{RAF}$, can be distinguished in the small angle X-ray scattering model. However, because our X-ray scans are taken at elevated temperatures in this work, the RAF has already been relaxed early in the heating cycle. So the two-phase assumptions of SAXS structural analysis are completely appropriate here.

Infrared studies were carried out in transmission mode with a Bruker Equinox Fourier Transform infrared spectrometer. The resolution was 4 cm^{-1}, and 32 scans were co-added to obtain a spectrum of each sample. The intensities of individual peaks were measured and analyzed by fitting them with Lorentz wave functions after baseline subtraction.

3. Results and discussion

3.1. Wide angle X-ray scattering (WAXS)

Fig. 2 shows the wide-angle X-ray scattering patterns in reflection mode at room temperature, of iPS amorphous

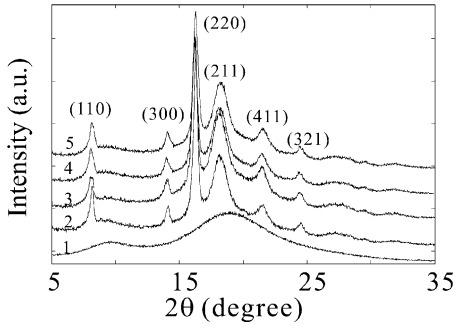

Fig. 2. Wide angle X-ray scattering intensity vs. scattering angle, 2θ, for $\lambda=0.154$ nm of iPS amorphous film (curve 1), and iPS cold-crystallized for 12 h at 150 °C (curve 2), 155 °C (curve 3), 160 °C (curve 4), and 165 °C (curve 5). Miller indices are given above the crystalline reflections [25].

bulk film (curve 1), and iPS films isothermally cold crystallized at 150 °C (curve 2), 155 °C (curve 3), 160 °C (curve 4), or 165 °C (curve 5). The X-ray scattered intensity is represented as a function of the scattering angle (2θ) at different crystallization temperatures. The amorphous scan shows two broad halos. The halo at upper scattering angle ($2\theta \approx 18.9°$, $q \approx 13\ nm^{-1}$) called the 'amorphous peak' [23,24] arises from phenyl-phenyl correlations, and the halo at lower scattering angle ($2\theta \approx 9.5°$, $q \approx 6\ nm^{-1}$) is the so-called 'polymerization peak' forming upon polymerization, which is due to intermolecular correlations of backbone atoms [23,24]. These halos both diminish in intensity as the crystals grow. The Miller indices of the crystalline reflections are indicated [25].

The WAXS crystallinity index was estimated from the ratio between the integrated Lorentz-corrected intensity of the crystalline peaks to the total integrated intensity of coherent scattering after subtraction of the incoherent background [18,19]. The degrees of crystallinity (ϕ_c) for all the samples obtained by WAXS are listed in Table 1.

3.2. FTir spectroscopy

Fig. 3 shows the FTir absorption spectra for the iPS amorphous film (curve 1), and iPS cold-crystallized for 12 h at 150 °C (curve 2), 155 °C (curve 3), 160 °C (curve 4), and 165 °C (curve 5). All the band assignments are based on the literature [26–29]. The band intensity at 981 cm^{-1} has a strong dependence on crystallinity, and has been treated as a crystalline band [30,31]. The band at 1026 cm^{-1} is due to the local vibrational mode associated with C–H deformations of the phenyl ring [27,31]. This band can serve as an internal standard because it is relatively intense and it does not change substantially during crystallization. In previous work [2], we obtained a linear relationship between crystallinity and intensity ratio of $I_{981\ cm^{-1}}/I_{1026\ cm^{-1}}$:

$$I_{(981\ cm^{-1})}/I_{(1026\ cm^{-1})} = 0.54\phi_c + 0.16 \quad (5)$$

By using this correlation, the crystallinity was estimated from the FTir spectrum, and these results are listed in Table 1.

Table 1
Crystalline, mobile amorphous, and rigid amorphous fractions for iPS as a function of crystallization temperature

T_c (°C)	150	155	160	165
ϕ_c (WAXS) (±0.02)	0.35	0.36	0.37	0.40
ϕ_c (DSC) (±0.01)	0.34	0.35	0.38	0.39
ϕ_c (FTir)[a] (±0.01)	0.34	0.35	0.37	0.38
ϕ_{MAF}[b] (±0.01)	0.54	0.53	0.51	0.50
ϕ_{RAF}[c] (±0.02)	0.12	0.12	0.11	0.10

[a] Determined from the band ratio $I_{981\ cm^{-1}}/I_{1026\ cm^{-1}}$ using Eq. (5).
[b] Determined from the heat capacity increment at the glass transition.
[c] Rigid amorphous fraction calculated based on a three-phase model: $\phi_{RAF} = 1 - \phi_c - \phi_{MAF}$.

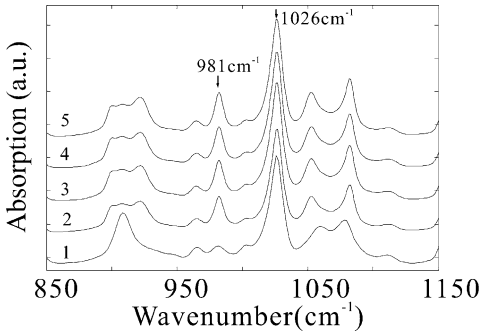

Fig. 3. FTir absorption spectrum of iPS amorphous film (curve 1), and iPS cold-crystallized for 12 h at 150 °C (curve 2), 155 °C (curve 3), 160 °C (curve 4), and 165 °C (curve 5). The two bands marked with arrows are the 981 and 1026 cm^{-1} bands.

3.3. Thermal analysis by standard DSC

Fig. 4 shows the standard DSC scan traces of iPS cold crystallized at $T_c = 155$ °C (a,b), 160 °C (c,d) and 165 °C (e,f) for $t_c = 12$ h. The glass transition temperature occurs at about 95–100 °C. Three endothermic peaks can be seen in the scan. The lowest temperature endotherm, labeled as the 'annealing peak' (T_a), will be discussed later in this work. The upper two endotherms (T_{m1} and T_{m2}) are the crystal melting peaks. The origin of double melting behavior has been suggested to be dual thermal stability distribution along one single lamella, due possibly to the irregular distribution of tacticity along a single macromolecular chain [11]. We observe that both T_a and T_{m1} have stronger dependence on super cooling (crystallization temperature, T_c). T_a occurs at about 15 °C above the crystallization temperature T_c, and both peak intensity and peak area for T_a decrease with increase of the crystallization temperature. T_{m1} also shifts to higher temperature as T_c increases. In contrast, the major melting peak T_{m2} almost remains the same for all crystallization temperatures. The degree of crystallinity is calculated by measuring the endothermic area using a sigmoidal baseline from:

$$\phi_c = \Delta H_f(m)/\Delta H_f^0 \quad (6)$$

where $\Delta H_f(m)$ is the measured heat of fusion and $\Delta H_f^0 = 86.6$ J/g is the heat of fusion of 100% crystalline iPS [33].

3.4. Three-phase structure in cold-crystallized iPS

Our previous work [2,3] showed that there are three fractions coexisting in cold-crystallized iPS, viz. the crystalline fraction, C, mobile amorphous fraction, MAF, and rigid amorphous fraction, RAF. The rigid amorphous fraction is due to strong coupling between mobile amorphous fraction and crystalline fraction, which does not contribute to the glass transition [34]. Thus, the only

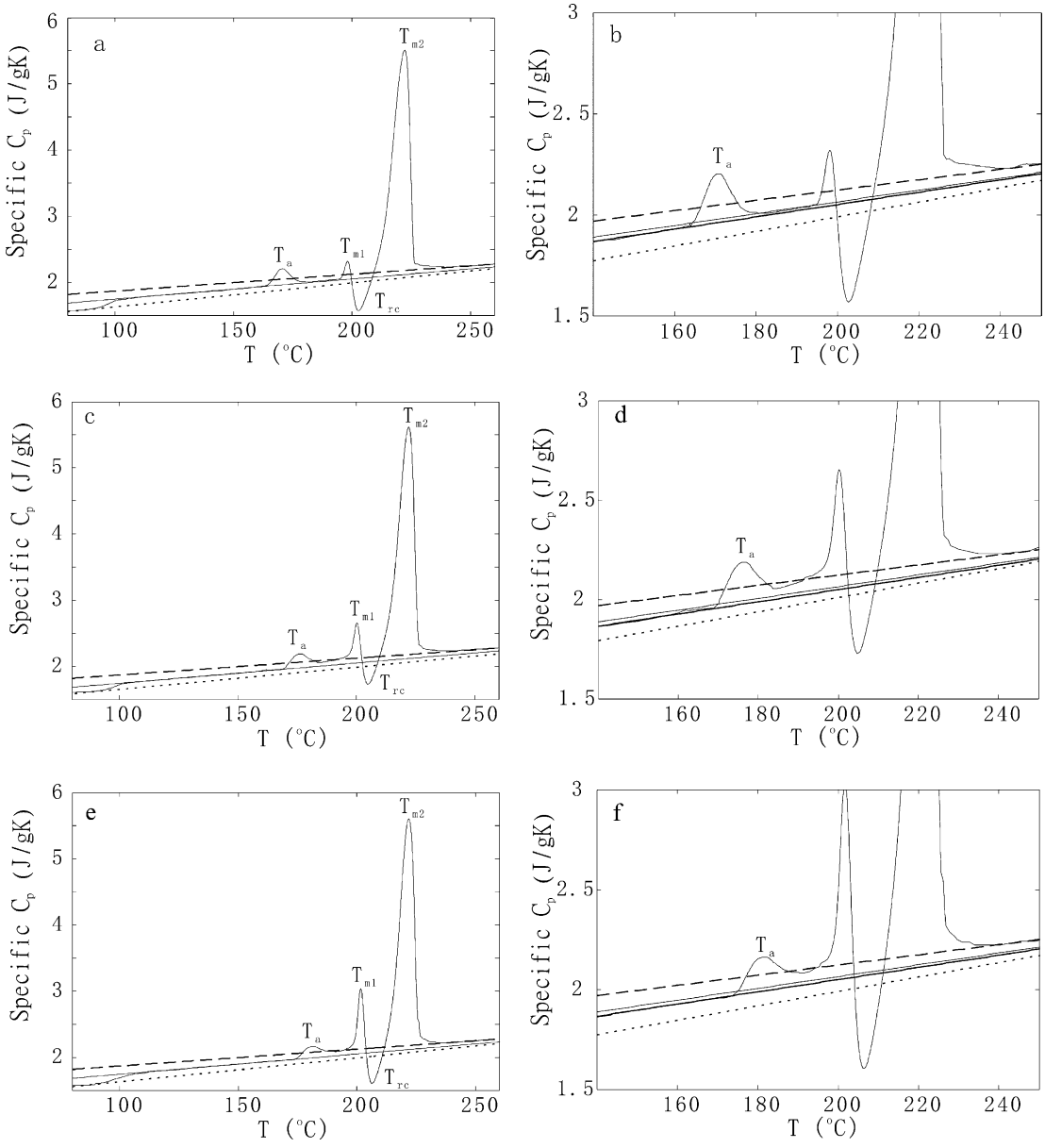

Fig. 4. Standard DSC scan ((a), (c), (e)—wide scaling; (b), (d), (f)—expanded scaling) showing specific heat capacity vs. temperature at heating rate of 10 °C/min, for iPS cold-crystallized for 12 h at: (a), (b) 155 °C, (c), (d) 160 °C, (e), (f) 165 °C. The dashed line is the heat capacity $C_p(T)|_{Liquid}$ of 100% liquid, while the dotted line is the heat capacity $C_p(T)|_{Solid}$ of 100% solid obtained from the ATHAS data bank [32]. In parts (a), (c), and (e), the solid line is the baseline heat capacity obtained from Eq. (12) based on the three-phase model, using phase fractions from Table 1. In parts (b), (d), and (f), the dark solid line represents the baseline heat capacity based on the three-phase model, while the light solid line indicates the baseline heat capacity based on the two-phase model. The correspondent phase fractions for each sample are listed in Table 1 (three-phase model) and Table 2 (two-phase model).

segments participating in the glass transition belong to the mobile amorphous fraction. The amount of the mobile amorphous fraction, ϕ_{MAF}, is obtained by measuring the heat capacity increment (ΔC_p) at the glass transition:

$$\phi_{MAF} = \Delta C_p^{SC}/\Delta_p^{AM} \tag{7}$$

where ΔC_p^{AM} is the heat capacity increment at the glass transition of 100% amorphous material, while ΔC_p^{SC} is the experimental result of the change of heat capacity at the glass transition for semicrystalline iPS samples. Then, amount of the rigid amorphous fraction, ϕ_{RAF}, can be deduced from [34]:

$$\phi_{RAF} = 1 - \phi_c - \phi_{MAF} \tag{8}$$

The results for the amounts of the different fractions under three-phase assumptions are shown in Table 1.

The heat capacities for both crystalline and glassy amorphous polymer are the same below T_g. Thus at temperatures below T_g the following equality holds:

$$C_p(T)|_{crystalline} = C_p(T)|_{MAF} = C_p(T)|_{RAF} = C_p(T)|_{Solid}, \quad T < T_g \tag{9}$$

When the system undergoes its glass transition, only the MAF participates in the process and above T_g the heat capacity of MAF follows the behavior of the liquid as:

$$C_p(T)|_{MAF} = C_p(T)|_{Liquid}, \quad T > T_g \tag{10}$$

while the other two portions (crystalline fraction and rigid amorphous fraction) remain in the solid state. Their heat capacity relation at temperatures within the range between T_g and T_a will be:

$$C_p(T)|_{crystalline} = C_p(T)|_{RAF} = C_p(T)|_{Solid}, \quad T_g < T < T_a \tag{11}$$

The $C_p(T)|_{Solid}$ and $C_p(T)|_{Liquid}$ were measured by standard DSC below T_g and above the upper melting point respectively. Our experimental data of $C_p(T)|_{Solid}$ and $C_p(T)|_{Liquid}$ match the values listed for atactic polystyrene in the ATHAS data bank within 1.5% in the measured temperature range.

By using each individual fraction and the correspondent heat capacity $C_p(T)$, we can construct the baseline heat capacity. The meaning of the 'baseline heat capacity' is: that heat capacity observed in the absence of any exothermic or endothermic phase transitions that would change the fractions (e.g. crystallization or melting) above the glass transition. For the semicrystalline sample, the baseline heat capacity at a given temperature, T, between T_g and T_a, is:

$$C_p(T) = (\phi_c + \phi_{RAF})C_p(T)|_{Solid} + (\phi_{MAF})C_p(T)|_{Liquid} \tag{12}$$

In Fig. 4(a), (c), and (e), the solid line is the baseline heat capacity. There is excellent agreement between the experimental data and the theoretical extrapolation using a three-phase model. In Fig. 4(a), (c), and (e) at temperatures between T_g and below the onset of the endothermic peaks, this agreement confirms the assumption of the three-phase model, with the baseline heat capacity obtained from Eq. (12), using the fractions as listed in Table 1.

3.5. Relaxation of RAF

In our previous work [1], we showed that the rigid amorphous fraction (RAF) was established at the crystallization temperature (T_c) for a well-crystallized iPS samples. Formation of RAF at T_c leads us to believe that RAF is stable at temperatures below T_c. Furthermore, heat capacity measurements above the melting point suggest that only one phase exists at high temperature, i.e. 100% liquid MAF. Therefore, the RAF must be relaxed at some temperature between T_c and the upper melting point. To provide further evidence for relaxation of RAF, Fig. 4(b), (d), and (f) shows the temperature dependent heat capacity $C_p(T)$ data in expanded scaling, for $T_c = 155$, 160, 165 °C, and for predictions based on the three-phase model (dark solid curve, 2) using fractions from Table 1. Also shown are the predictions based on a two-phase model (light solid curve, 1). The two-phase model assumption is that the rigid amorphous fraction has relaxed to become mobile amorphous. In this case, $\phi_{MAF} = 1\text{-}\phi_c$. The fractions under the two-phase model assumptions are listed in Table 2.

In Fig. 4(b), (d), and (f) at temperatures below the annealing peak, experimental C_p matches the three-phase model baseline. In Fig. 4(b) ($T_c = 155$ °C), at temperature just above the annealing peak, the system approaches to the two-phase model, in which only crystals and liquid (MAF) exist. Thus, as temperature increases from below T_a to above T_a, the system exhibits a transition from three-phase to two-phase, with fractions given in Table 2. Such a transition turns the RAF into an identical amount of MAF. Using FTir, WAXS, and standard DSC scanning, the crystalline fraction appears to be unaffected by the transition of RAF into MAF, at least within the error limits of the crystallinity measurement. It is possible that a tiny amount of crystals, within the error limits, melts at T_a. However, as we demonstrated before [35], it is not possible for the entire endotherm area at T_a to arise from crystal melting.

Therefore, the annealing peaks in Fig. 4(a), (c), and (e) represent the relaxation of rigid amorphous fraction, which transforms RAF into equilibrium liquid without detectable melting of the crystals. The relaxation of RAF occurs as a sigmoidal change in the baseline heat capacity, accompanied by excess enthalpy. We also see that, in Fig. 4(d) ($T_c = 160$ °C) and Fig. 4(f) ($T_c = 165$ °C), for these two samples the experimental curves do *not* return to the two-phase model baseline above T_a. This indicates that, as T_a increases and becomes nearer to the melting temperature range of the crystals, melting of crystals may occur at, or immediately following the relaxation of the RAF [10].

3.6. Melting behavior of iPS

3.6.1. Double reversing melting

Several polymers show small reversibility of melting in quasi-isothermal TMDSC measurements conducted by Wunderlich [36–40] and others [41–43]. Based on our work, isotactic polystyrene is the first linear macromolecule that demonstrates double reversing melting [1]. Fig. 5 shows a quasi-isothermal TMDSC scan of iPS crystallized at

Table 2
Crystalline and mobile amorphous fractions for iPS as a function of crystallization temperature using two-phase model assumptions

T_c (°C)	150	155	160	165
ϕ_c[a]	0.34	0.35	0.38	0.39
ϕ_{MAF}	0.66	0.65	0.62	0.61

Two-phase model assumes $\phi_{MAF} = 1 - \phi_c$ and $\phi_{RAF} = 0$.
[a] From DSC measurement.

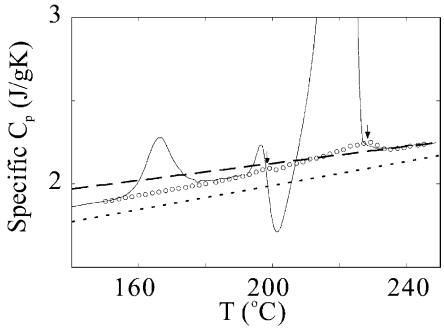

Fig. 5. The specific total heat capacity vs. temperature of iPS cold crystallized at 150 °C for 12 h by standard DSC scan (solid curve) and the reversing heat capacity obtained from quasi-isothermal TMDSC (*o*). The dashed line is the heat capacity $C_p(T)|_{Liquid}$ of 100% liquid, while the dotted line is the heat capacity $C_p(T)|_{Solid}$ of 100% solid obtained from the ATHAS data bank [32].

150 °C for 12 h. In Fig. 5, the solid curve is the specific total heat capacity obtained for a standard DSC scan, and the open circle data points are the specific reversing heat capacity by quasi-isothermal TMDSC measurements. The dashed and dotted lines are the heat capacity of iPS liquid and solid, respectively. There are two small peaks clearly seen in the reversing heat capacity data points, which are marked with down arrows. These two small reversing melting peaks are located on the higher temperature side of their correspondent melting peaks (T_{m1}, T_{m2}) in standard DSC scan (solid curve).

The common explanation of reversible melting of macromolecules is that in the melting region, some portions of molecular chain remain crystallized. These portions of the chain are called the 'molecular nucleus' which is the origin of reversible melting [44]. Once the temperature modulation is applied, the non-crystallized portion of the molecular chain, which is connected to the molecular nucleus, will crystallize in the cooling cycle and melt again in the following heating cycle. The reversibility of melting and crystallization could be retained until increasing the temperature destroys all the molecular nuclei [44]. Certainly, such a mechanism could be applied as well to describe the origin of reversing melting in iPS.

By considering the melting behavior of iPS, our observation of double reversing melting supports the recent proposal of Petermann [11] that the double melting of iPS is due to non-uniform thermal stability distribution along one single lamella, which is possibly caused by uneven tacticity distribution. By using TEM, Petermann observed the lamellae became broken at T_{m1}, and the broken lamellae 'repaired' themselves indicating recrystallization, and then melted completely at T_{m2}. Our quasi-isothermal TMDSC experiments support this proposal, that at T_{m1} some portions of lamellae melt. A reversing melting event was found to be associated with T_{m1} in quasi-isothermal TMDSC measurements reflected by the lowest reversing melting peak in the quasi-isothermal TMDSC data. When the temperature continues to increase to T_{m2}, all the remaining portions of the lamellae melt and another reversing melting event was found in quasi-isothermal TMDSC experiments, as demonstrated by the highest reversing melting peak. Between the two peaks, it appears that the reversing melting might be lost, since there is probably no corresponding non-reversing melting event occurring at that temperature location [41,42]. The samples crystallized at higher temperatures ($T_c = 155$, 160, 165 °C) also show very similar dual reversing melting signatures in quasi-isothermal TMDSC experiments, but in the interests of brevity, we do not present them here.

3.6.2. Annealing of crystal lamellae during heating

Since the folded chain crystal structure is not in thermodynamic equilibrium, upon heating, annealing, reorganization (recrystallization) and melting may occur. The effect of annealing has been used to explain the fact that the reversing melting peak in quasi-isothermal TMDSC experiments is always located on the higher temperature side of the melting peak in standard DSC scan [45]. The effect of annealing was also found in iPS, in our previous work [1]. For example, in iPS sample crystallized at 140 °C for 12 h, there is only one melting peak found in a standard DSC scan. However, such a sample still exhibited dual reversing melting behavior [1]. While two small peaks are seen in quasi-isothermal TMDSC experiments, there is only one major melting peak (T_{m2}) found in the standard DSC scan.

To explore the origin of such behavior, an interrupted quasi-isothermal measurement was conducted in standard DSC mode. The detailed procedure is given by the following sequence: (1) the sample is first heated to 140 °C at 10 °C/min (2) the sample is held isothermally for 20 min and then the temperature is increased by 2.5 °C (3) step 2 is repeated until the temperature reaches a desired end point, T_{end} (4) then the sample is heated to melting at 10 °C/min. Except for modulation, step 2 replicates the annealing that would occur in the quasi-isothermal experiment.

Fig. 6 shows the serial scans as a function of specific T_{end}: (1) 145 °C; (2) 170 °C; (3) 190 °C; (4) 200 °C; and (5)

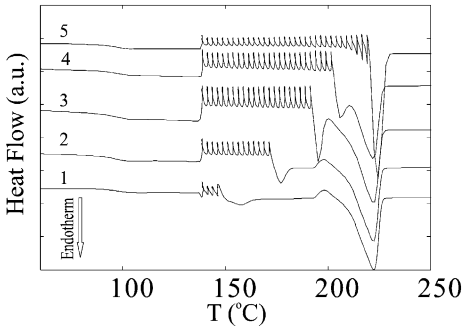

Fig. 6. Scan of interrupted quasi-isothermal process in standard DSC mode of iPS cold crystallized at 140 °C for 12 h. The detailed description of the treatment is given in the text. The curve represents different T_{end}: (1) 145 °C; (2) 170 °C; (3) 190 °C; (4) 200 °C; (5) 220 °C.

220 °C. In Fig. 6, the abscissa is temperature, the ordinate is heat flow, and the endotherms are indicated by downward reflection. The oscillations in the heat flow represent transients seen when the instrument changes to isothermal mode after each step-change in temperature.

The results of these scans support the point of view of the effect of annealing by consideration of the following features. First, the endotherm at T_{m1} is strongly enhanced when the T_{end} increases, and T_{m1} shifts to a higher temperature. This observation suggests that the lowest reversing melting peak in quasi-isothermal TMDSC scan is not correlated to the original standard DSC scan (which in fact does not show an endotherm at T_{m1}) but is associated with the lowest melting peak occurring after serial stepwise annealing (i.e. the first endotherm of scan (3) in Fig. 6). Second, T_{m2} shifts to higher temperature with increasing T_{end}, indicating that the portion of crystalline lamellae with higher thermal stability experiences a perfection process during the stepwise scan. The melting point of the lamellae is related to lamellar thickness by the Hoffman-Weeks relationship [46].

We suspect there is possible lamellar thickening occurring during stepwise heating. To verify this suggestion, real time SAXS experiments were performed, using a heating process similar to that used in the quasi-isothermal TMDSC experiments, with temperature increment, $\Delta T = 2.5$ °C, and holding time of 20 min. During each 20-min step, four frames of data were taken, such that each frame integrated the scattering intensity for 5 min. Only the last frame of data (last 5 min of isothermal holding) at each temperature step is presented. Fig. 7(a) displays the scheme of this experiment, in which the abscissa is time (min) and the ordinate is temperature (°C). Fig. 7(b) shows the SAXS intensity vs. q-vector of the sample at different selected temperatures: 145, 180, 212, and 220 °C. The one-dimensional electron density correlation function is used to determine the scattering parameters including the long period, L^{MAX} and the phase thickness, z_2, determined according to Fig. 1. In the two-phase lamellar stack model, the other phase thickness, z_1, is simply calculated by Eq. (2).

Fig. 8(a)–(d) shows the scattering invariant, Q, long period, L^{MAX}, smaller phase thickness, z_2, and larger phase thickness, z_1, respectively, versus temperature. As shown in Fig. 8(a), the scattering invariant increases with temperature from $T = 145$ to 190 °C, which suggests that further crystallization occurs within this temperature range. This behavior is normal for a sample crystallized at a relatively low temperature of 140 °C. Within this temperature range (145–190 °C), we also found that the long period L^{MAX} steadily decreases. When the temperature is above 190 °C, melting events are signified by decrease of the scattering invariant and increase of the long period.

From the correlation function, the phase thickness of z_1 and z_2 are obtained and are plotted in Fig. 8(c), (d), respectively. According to Babinet's principle of reciprocity [22], we cannot determine whether z_1 or z_2 represents the crystal phase thickness. Additional information is provided by the temperature dependence of these two lengths. In Fig. 8(d), the larger phase thickness, z_1, decreases during the further crystallization stage (145–190 °C) and increases in the melting stage (above 190 °C). This observation suggests the larger phase thickness should be attributed to amorphous phase, so that $L_a = z_1$, and the smaller phase thickness, should be attributed to the crystalline phase, so that $L_c = z_2$. This assignment is also in accordance with a larger amorphous phase fraction obtained in thermal, FTir and WAXS analyses. In Fig. 8(c), the lamellar thickness L_c always increases with temperature until the temperature rises above 215 °C, at which point we could not obtain a good analysis because the long period is moving into the beam stop region, suggesting only isolated crystals are left. The time dependence of the SAXS structural parameters lends support to our suggestion that the stepwise heating process anneals (thickens) the crystal lamellae, resulting in the melting point shifting to a higher temperature.

3.6.3. Model of melting iPS crystal lamellae

Our previous work using quasi-isothermal TMDSC on iPS bulk film [1] supported Petermann's [11] proposal regarding the multiple melting of iPS. Petermann [11] suggested that the origin of multiple melting of iPS is due to a non-uniform thermal stability distribution along one single lamella, possibly due to uneven tacticity distribution. We believe the lowest reversing melting peak in the

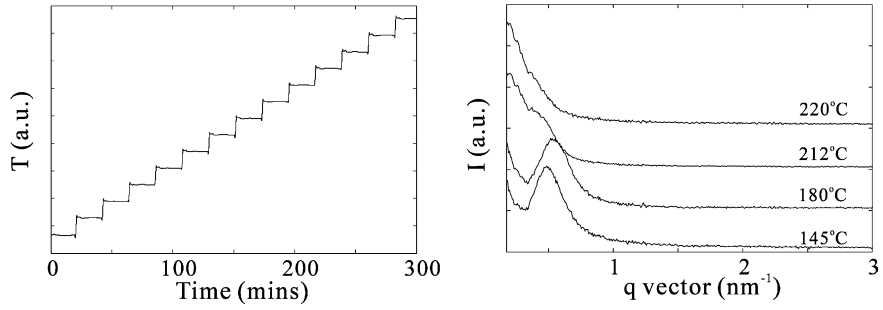

Fig. 7. (a) Temperature vs. time during the real-time SAXS measurements. The heating process is realized by a stepwise increase of temperature, with $\Delta T = 2.5$ °C per step and holding time = 20 min. (b) SAXS intensity vs. q-vector of iPS sample at different selected temperatures as indicated. Each curve represents the intensity for the last 5 min of holding at the given temperature.

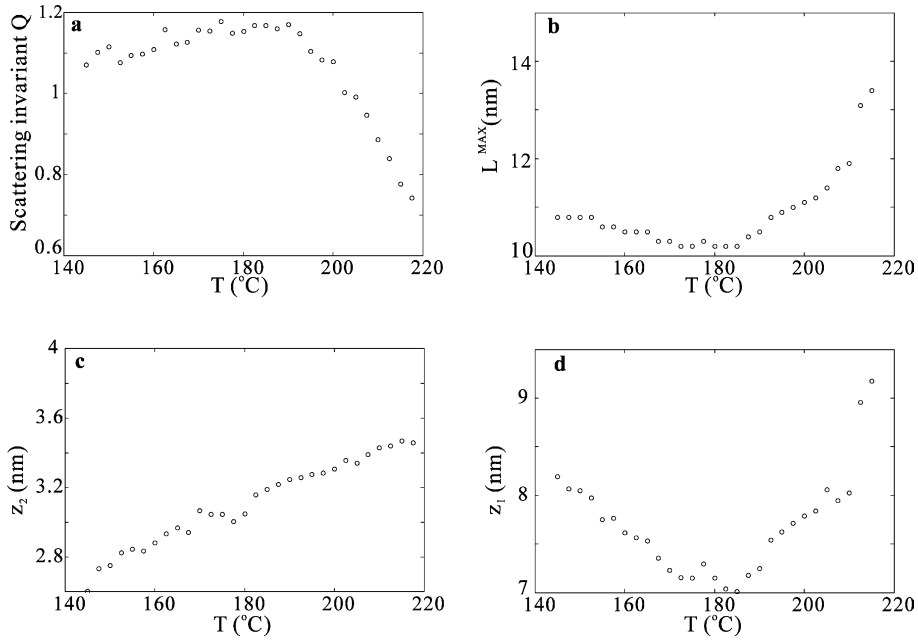

Fig. 8. Real-time SAXS parameters as functions of temperature during stepwise heating. (a) Scattering invariant Q. (b) Long period L^{MAX}. (c) Smaller phase thickness, z_2, the crystal thickness. (d) Larger phase thickness, z_1, the amorphous phase thickness. L^{MAX} and z_2 are determined according to Fig. 1. z_1 is found from Eq. (2).

quasi-isothermal measurements is associated with the melting of portions of lamellae with low stability, and the uppermost reversing melting peak corresponds to the remaining lamellae with high thermal stability [1]. In this work, by combining standard DSC, quasi-isothermal TMDSC, interrupted quasi-isothermal DSC, and real time SAXS observations on iPS bulk samples, we provided a model to explain the mechanism of multiple melting of iPS lamellae grown by cold-crystallization. The purpose of this model is to correlate the TEM observations of Petermann [11] with our observations of dual reversing melting endotherms.

From the discussion above, we know that annealing occurs during heating of cold-crystallized iPS films, and the level of annealing (crystal perfection after annealing) depends on heating rate, with standard DSC providing modest linear heating rate, and quasi-isothermal TMDSC providing an extremely low heating rate (limit $q \rightarrow 0$). Based on this point of view, we propose a model [1] of the melting mechanism of iPS based on the transmission electron microscopy observations of Petermann [11]. By using TEM, Petermann [11] observed that an individual lamella became broken when the temperature reached T_{m1}, and the remaining parts of the lamella became completely melted after $T = T_{m2}$. In between, reorganization was observed, and the broken lamella was 'repaired'. However, this suggestion does not fully explain two of our observations. First, the uppermost DSC melting peak (T_{m2}) is crystallization temperature independent, at the scan rates used in standard DSC. Second, for a sample cold-crystallized at lower temperature (140 °C), the lowest melting peak, T_{m1}, is seen in quasi-isothermal TMDSC measurement but it is not seen in standard DSC scanning.

By considering the effect of annealing, we suggest the following model to describe the multiple melting behavior of iPS bulk sample seen in the standard DSC scan (Fig. 9(a)) and the quasi-isothermal TMDSC experiment (Fig. 9(b)). In Fig. 9(a), the temperature increases at a limited heating rate. The four schematic lamellae are interpreted as follows: (1) the lamella is intact for $T < T_{m1}$; (2) at T_{m1}, the lowest stability portion of the lamella melts, while the more stable portions become annealed; (3) at the recrystallization exotherm, T_{rc}, the lamella is repaired by recrystallization, and annealing continues; (4) remaining portions of the lamella with highest thermal stability melt finally as temperature rises above T_{m2}. The arrow on the right side of Fig. 9(a) indicates the effect of annealing on the crystal fold period. Annealing during the heating thickens lamellae and consequently shifts the melting point to higher temperature.

In Fig. 9(b), the temperature increases in a stepwise manner (limit $q \rightarrow 0$). The notation of T'_{m1}, T'_{m2} indicates the reversing melting peak position observed in the quasi-isothermal TMDSC experiment. The four schematic lamellae are interpreted as follows: (1) at T'_{m1}, the lowest stability portion of the lamella melts, and demonstrates a small reversibility of melting under temperature modulation, while the more stable portions become annealed. A small crystal with molecular nucleus remains (for example, as depicted in Fig. 9(c)); (2) as the temperature increases above T'_{m1} the small crystal with molecular nucleus melts;

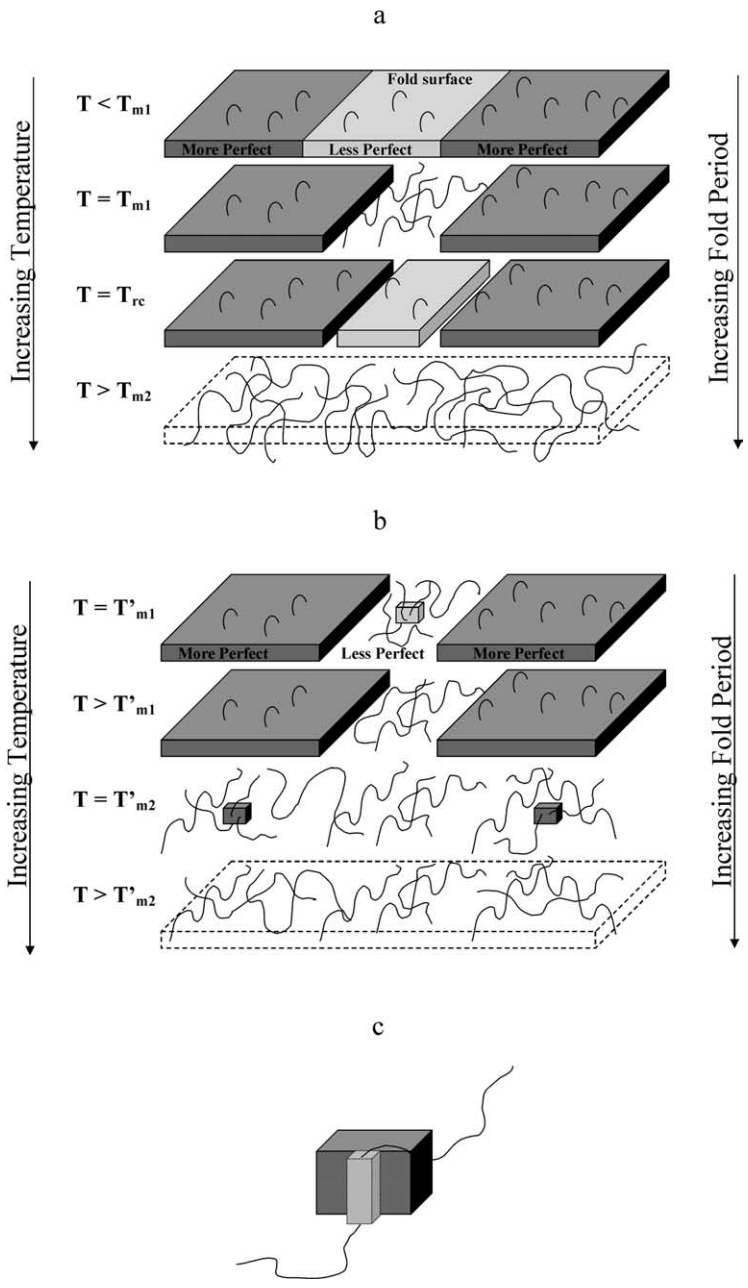

Fig. 9. Scheme of the model of the melting of a single lamella of cold crystallized iPS bulk sample as seen in: (a) standard DSC scan at limited heating rate; and, (b) quasi-isothermal TMDSC scan with $q \rightarrow 0$ (c) enlarged view of one of the small crystals in part (b), showing an attached molecular nucleus. According to the suggestion of Petermann [11] the lamellae in (a) and (b) are depicted with regions of different thermal stability (perfection), called 'more perfect' (dark shaded lamellae) and 'less perfect' (light shaded lamellae). Temperature increases downward, from top to bottom. The unprimed temperatures refer to thermal transitions observed in standard DSC; the primed temperatures refer to thermal transitions observed in quasi-isothermal TMDSC.

(3) at T'_{m2}, the second peak of reversing melting is observed suggesting that most of the remaining portions of lamellae melt, leaving a small crystal with molecular nucleus; (4) all remaining crystals with their molecular nuclei melt when the temperature rises above T'_{m2}, and the system becomes homogeneous liquid.

During normal DSC scanning, in Fig. 9(a), in the temperature range from T_{m1} to T_{m2}, reorganization (recrystallization) occurs, and the just-melted portion of the lamella crystallizes again and becomes more perfect crystal, having longer fold period and higher melting temperature. The other portions of the lamella, with higher thermal stability, also experience annealing. The effect of annealing is explained on the right side of Fig. 9(a), (b).

At higher temperatures, the crystallized molecules rearrange themselves and become thicker lamellae. This suggestion is supported by the observation of lamellar thickening in the real-time SAXS experiments during the stepwise heating. Therefore, the endothermic peak occurring at T_{m2} in a standard DSC scan is due to melting of

annealed crystal lamellae that have been thickened during the heating. This reorganization could be the reason why T_{m2} is independent of crystallization temperature. It would be valuable to determine the ultimate rate of reorganization possible in this material, under conditions of very fast heating. Studies of iPS crystals under rapid heating rate conditions available with nanocalorimetry [47,48] are currently underway by Schick's group [49].

4. Conclusion

The transitions from solid to liquid in iPS have been studied using heat capacity measurements and X-ray scattering. By extending the range of crystallization temperatures, we are able to produce the three phase fractions in iPS such that not only is the relaxation of RAF distinguished from melting, but also the dual endothermic features are clearly maintained. A three-phase model, comprising the mobile amorphous (MAF), rigid amorphous (RAF) and crystalline phases, is appropriate to interpret the structure of cold-crystallized isotactic polystyrene (iPS). The specific heat capacity, $C_p(T)$ was measured by DSC, and the three-phase model fits the experimental baseline heat capacity very well from temperatures just above the glass transition to just below the temperature of relaxation of the rigid amorphous fraction. For all samples studied, the transition of RAF, from solid-like to liquid like, was found to be an enthalpy involved process, which occurs at a temperature T_a marking the first endothermic event seen in standard DSC measurements.

We studied the reversing melting behavior of iPS, using quasi-isothermal TMDSC. For cold-crystallized iPS, multiple reversible melting peaks were observed, even when only a single melting peak could be seen in standard DSC scanning. The very slow effective heating rates of the quasi-isothermal method result in annealing of lamellar crystals. This results in thickening of the lamellae and an increase of the uppermost melting endotherm temperature, T_{m2}. Companion studies of the effects of annealing were carried out using SAXS to demonstrate that the transition of solid crystalline phase to liquid melt occurs through a complex process involving partial melting, rearranging (annealing), reorganization (recrystallization), and final melting.

Acknowledgements

The National Science Foundation, Polymers Program of the Division of Materials Research supported this research through grant DMR - 0100646. A portion of this work was carried out at the Advanced Polymers Beamline, X27C, at Brookhaven National Laboratory, National Synchrotron Light Source.

References

[1] Xu H, Cebe P. Macromolecules 2004;37:2797.
[2] Xu H, Ince BS, Cebe P. J Polym Sci, Polym Phys Ed 2003;41:3026.
[3] Natesan B, Xu H, Ince BS, Cebe P. J Polym Sci, Polym Phys Ed 2004; 42:777.
[4] Song M. J Appl Polym Sci 2001;81:2779.
[5] Cheng SZD, Pan R, Wunderlich B. Makromol Chem 1988;189:2443.
[6] Huo PP, Cebe P. Macromolecules 1992;25:902.
[7] Cheng SZD, Cao MY, Wunderlich B. Macromolecules 1986;19:1868.
[8] Huo PP, Cebe P. Colloid Polym Sci 1992;270:840.
[9] Lu SX, Cebe P. Polymer 1996;37:4857.
[10] Schick C, Wurm A, Mohammed A. Thermochim Acta 2003;396:119.
[11] Liu T, Petermann J. Polymer 2001;42:6453.
[12] Crist B. Macromolecules 2003;36:4880.
[13] Kong Y, Hay JN. Polymer 2003;44:623.
[14] Matsuda H, Aoike T, Uehara H, Yamanobe T, Komota T. Polymer 2001;42:5013.
[15] Ishikiriyama K, Wunderlich B. J Therm Anal 1997;50:337.
[16] Hohne GWH, Merzlyakov M, Schick C. Thermochim Acta 2002; 391(1-2):51.
[17] Merzlyakov M, Hohne GWH, Schick C. Thermochim Acta 2002; 391(1-2):69.
[18] Blundell DJ, Osborn BN. Polymer 1983;24:953.
[19] Balta-Calleja FJ, Vonk CG. X-ray scattering of synthetic polymers. Amsterdam: Elsevier; 1989.
[20] Vonk CG, Kortleve G. Kolloid Z Z Polym 1967;220:19.
[21] Strobl GR, Schneider M. J Polym Sci, Polym Phys Ed 1980;18:1343.
[22] Glatter O, Kratky O. Small angle X-ray scattering. London: Academic Press; 1982.
[23] Ayyagari C, Bedrov D, Smith GD. Macromolecules 2000;33:6194.
[24] Mitchell GR, Windle AH. Polymer 1984;25:906.
[25] Natta G, Corradini P, Bassi IW. Naovo Cimento 1960;15:68.
[26] Kobayashi M, Tsummura K, Tadokoro H. J Polym Sci, Polym Phys Ed 1968;6:1493.
[27] Kobayashi M, Akita K, Tadokoro H. Makromol Chem 1968;118:324.
[28] Painter PC, Koeing JL. J Polym Sci, Polym Phys Ed 1977;15:1885.
[29] Kobayashi M, Nakaoki T, Ishihara N. Macromolecules 1990;23:78.
[30] Nakoaki T, Kobayashi M. J Mol Struct 1991;242:315.
[31] Kobayashi M, Nakaoki T. Macromolecules 1990;23:78.
[32] ATHAS data bank, http://web.utk.edu/~athas/databank/, Pyda M. editor; 1994.
[33] Brandup J, Immergut EH, Grulke EA, Abe A, Bloch DR. Polymer handbook. New York: Wiley Interscience; 1999.
[34] Suzuki H, Grebowicz J, Wunderlich B. Br Polym J 1985;17:1.
[35] Xu H, Cebe P. Preprints of the American Chemical Society, Division of Polymeric Materials: Science and Engineering, 2005;93 in press.
[36] Okazaki I, Wunderlich B. Macromolecules 1997;30:1758.
[37] Ishikiriyama K, Wunderlich B. Macromolecules 1997;30:4126.
[38] Androsch R, Wunderlich B. Macromolecules 2001;34:5950.
[39] Pyda M, Di Lorenzo M, Pak J, Kamasa P, Buzin A, Grebowicz J, et al. J Polym Sci, Polym Phys Ed 2001;39:1565.
[40] Di Lorenzo M, Pyda M, Wunderlich B. J Polym Sci, Polym Phys Ed 2001;39:1594.
[41] Androsch R, Wunderlich B. J Polym Sci, Polym Phys Ed 2003;41: 2157.
[42] Androsch R, Wunderlich B. J Polym Sci, Polym Phys Ed 2003;41: 2039.
[43] Wurm A, Merzlyakov M, Schick C. Colloid Polym Sci 1998;276:289.
[44] Wunderlich B, Mehta A. J Polym Sci, Polym Phys Ed 1974;12:255.
[45] Schick C, Merzlyakov M, Wunderlich B. Polym Bull 1998;40:297.
[46] Hoffman JD, Weeks JJ. J Res Natl Bur Stand (US) 1962;A66:13.
[47] Minakov AA, Mordvintsev DA, Schick C. Polymer 2004;45:3755.
[48] Adamovsky SA, Minakov AA, Schick C. Thermochim Acta 2003; 403:55.
[49] Private correspondence with Prof Christoph Schick; 2004.